AFRL-RV-PS-
TR-2014-0037

IONOSPHERE-THERMOSPHERE COUPLING – DATA ANALYSIS AND NUMERICAL SIMULATION STUDY

Christos Christodoulou

The University of New Mexico
1 University of New Mexico
Albuquerque, NM 87131

12 December 2013

Final Report

AIR FORCE RESEARCH LABORATORY
Space Vehicles Directorate
3550 Aberdeen Ave SE
AIR FORCE MATERIEL COMMAND
KIRTLAND AIR FORCE BASE, NM 87117-5776

DTIC COPY

NOTICE AND SIGNATURE PAGE

Using Government drawings, specifications, or other data included in this document for any purpose other than Government procurement does not in any way obligate the U.S. Government. The fact that the Government formulated or supplied the drawings, specifications, or other data does not license the holder or any other person or corporation; or convey any rights or permission to manufacture, use, or sell any patented invention that may relate to them.

This report was cleared for public release by the 377 ABW Public Affairs Office and is available to the general public, including foreign nationals. Copies may be obtained from the Defense Technical Information Center (DTIC) (http://www.dtic.mil).

AFRL-RV-PS-TR-2014-0037 HAS BEEN REVIEWED AND IS APPROVED FOR PUBLICATION IN ACCORDANCE WITH ASSIGNED DISTRIBUTION STATEMENT.

//SIGNED//	//SIGNED//
Dr. Cheryl Huang	Edward J. Masterson, Colonel, USAF
AFRL/RVBXP Program Manager	Chief, Battlespace Environment Division

This report is published in the interest of scientific and technical information exchange, and its publication does not constitute the Government's approval or disapproval of its ideas or findings.

REPORT DOCUMENTATION PAGE

Form Approved
OMB No. 0704-0188

1. REPORT DATE *(DD-MM-YYYY)*	**2. REPORT TYPE**	**3. DATES COVERED** *(From - To)*
12-12-2013	Final Report	14 Nov 2012 to 18 Oct 2013

4. TITLE AND SUBTITLE
Ionosphere-Thermosphere Coupling – Data Analysis and Numerical Simulation Study

5a. CONTRACT NUMBER
FA9453-13-1-0228

5b. GRANT NUMBER

5c. PROGRAM ELEMENT NUMBER
61102F

6. AUTHOR(S)
Christos Christodoulou

5d. PROJECT NUMBER
3001

5e. TASK NUMBER
PPM00019201

5f. WORK UNIT NUMBER
EF121720

7. PERFORMING ORGANIZATION NAME(S) AND ADDRESS(ES)
The University of New Mexico
1 University of New Mexico
Albuquerque, NM 87131

8. PERFORMING ORGANIZATION REPORT NUMBER

9. SPONSORING / MONITORING AGENCY NAME(S) AND ADDRESS(ES)
Air Force Research Laboratory
Space Vehicles Directorate
3550 Aberdeen Avenue SE
Kirtland AFB, NM 87117-5776

10. SPONSOR/MONITOR'S ACRONYM(S)
AFRL/RVBXP

11. SPONSOR/MONITOR'S REPORT NUMBER(S)
AFRL-RV-PS-TR-2014-0037

12. DISTRIBUTION / AVAILABILITY STATEMENT
Approved for public release; distribution is unlimited. (377ABQ-2014-0213 dtd 31 Mar 2014)

13. SUPPLEMENTARY NOTES

14. ABSTRACT

The well-known Fang parameterizations of monoenergetic particle impact ionization have been applied to the complex energy spectra measured by the DMSP F16 satellite to calculate the ionization rates from electron and ion precipitations for a northern hemisphere pass from 0030 UT to 0106 UT on August 6, 2011. The particle impact ionization rates using the Fang parameterizations showed a clear enhancement at F-region altitudes in the polar cap region mainly due to the low-energy precipitating electrons. The general circulation models (GCMs), the NCAR Thermosphere-Ionosphere-Electrodynamics General Circulation Model (TIE-GCM) and the Global Ionosphere Thermosphere Model (GITM) do not capture the observed features shown in the total particle ionization rate when applying the Fang parameterizations to DMSP measurements. The difference between the GCM simulations and those obtained by the Fang models, applied to DMSP data, is due to the difference of both the inputs to the models and the parameterization of the ionization rates.

15. SUBJECT TERMS
particle impact ionization, ionization rate, ionopshere-thermosphere coupling, Poynting Flux

16. SECURITY CLASSIFICATION OF:			**17. LIMITATION OF ABSTRACT**	**18. NUMBER OF PAGES**	**19a. NAME OF RESPONSIBLE PERSON**
a. REPORT	**b. ABSTRACT**	**c. THIS PAGE**			Dr. Cheryl Huang
Unclassified	Unclassified	Unclassified	Unlimited	28	**19b. TELEPHONE NUMBER** *(include area code)*

Standard Form 298 (Rev. 8-98)
Prescribed by ANSI Std. 239.18

This page is intentionally left blank.

TABLE OF CONTENTS

LIST OF FIGURES

1. Summary

We have evaluated ionization due to particle precipitation during a magnetic storm. The ionization due to particle precipitation measured along a Defense Meteorological Satellite Program (DMSP) F16 satellite trajectory was determined using a new model . During the DMSP F16 pass over the northern hemisphere from 0030 UT to 0106 UT on August 6, 2011, a broad and strong enhancement of Poynting flux in the polar cap latitudes was observed, which is comparable in magnitude to those in the auroral zones. This high-latitude Poynting flux enhancement is associated with the particle precipitation enhancement in the polar cap. Besides the Poynting flux and particle spectra data, the ion convection data were also available for this F16 pass, providing an opportunity to assess the storm event. The particle impact ionization results were put into different atmospheric models (NRLMSISE-00 [Picone et al., 2002], TIE-GCM, and GITM) to examine their geoeffectiveness. The summation of both electron and ion impact ionization rates illustrate the enhanced total ionization in auroral and polar cap regions that is associated with the enhanced Poynting flux during this satellite pass. Results indicate that the default models used to calculate ionization do not adequately represent the true ionization at high latitudes.

2. Introduction

Electron and proton precipitation constitutes an important ionization and heating source of the Earth's ionosphere-thermosphere (I-T) system, particularly at high latitudes. Besides the energetic particle precipitation in the auroral zone, there is relatively low-energy particle precipitation through open field lines in the polar cusp [Heikkila and Winningham, 1971; Frank, 1971] and over the polar cap region [Winningham and Heikkila, 1974; Zhang et al., 2007]. The spatially homogeneous precipitation of soft particles in the polar cap is called polar rain. Previously, most attention has been paid to particle precipitation in the auroral zone [Rees et al., 1983; Roble and Ridley, 1987; Newell et al., 2009; Luan et al., 2010], and soft particle precipitation in the cusp region has not received attention until recently [Lühr et al., 2004; Crowley et al., 2010; Knipp et al., 2011; Deng et al., 2013]. Since precipitating electrons in the

polar cap are typically soft (with energy of a few hundred eVs) and weak (with energy flux ranging from 0.001 to 0.01 erg/cm2/s), their resulting ionization and heating effects are often considered negligible. However, this is not always true.

Very recently, Huang et al. [2013] analyzed the thermospheric energy budget during a moderate storm occurring on August 5-6, 2011, and found that the ionospheric energy in the auroral zone cannot account for the thermosphere heating. In addition, the Traveling Atmospheric Disturbances (TADs) propagating from high latitudes towards the equator indicate that the source of Joule heating is polewards of 83□ and 72□ magnetic latitudes in the northern and southern hemispheres, respectively. These findings suggest that the thermosphere may be primarily energized at polar cap latitudes, and there is a potential underestimation of the ion production in the polar cap, which may leads to the underestimation of electron density, Pedersen conductivity, Joule heating, and finally result in a poor understanding of the I-T system. Therefore, it is important to revisit the role of particle precipitation in the polar cap, specifically by applying a global model with appropriately calculated particle impact ionization rates.

There have been several parameterizations for calculating electron impact ionization rates, e.g. Lazarev [1967], Roble and Ridley [1987], Frahm et al. [1997], Fang et al. [2008] and Fang et al. [2010, hereafter Fang2010]. Large-scale global circulation models (GCMs) have to rely on these empirical models to quickly and self-consistently calculate and incorporate the particle impact ionization. For example, the National Center for Atmospheric Research (NCAR) Thermosphere-Ionosphere-Electrodynamics General Circulation Model (TIE-GCM) and the Michigan Global Ionosphere Thermosphere Model (GITM) adopt the Roble and Ridley [1987] and Frahm et al. [1997] methods, respectively. However, these two empirical ionization calculation methods are based on simplified calculations and are not appropriate to calculate the effects from precipitating soft particles with energy of a few hundred eVs [Fang2010]. In order to accurately represent soft particle precipitation in global modeling, we employ the newly developed parameterizations of Fang2010 and Fang et al. [2013, hereafter Fang2013] to calculate electron and ion impact ionization rates, respectively. Based on complicated, physics-based particle transport models, these new methods provide an accurate and fast means to estimate the ionization rate altitude profiles from incident monoenergetic 100 eV to 1 MeV particles. In

particular, the parameterizations give satisfactory results for precipitating soft particles with energy as low as 100 eV, which are otherwise not obtainable by previous methods.

In this study, we investigated the ionization due to particle precipitation along a Defense Meteorological Satellite Program (DMSP) F16 satellite trajectory across the northern hemisphere during a moderate storm in August 2011. During the DMSP F16 pass over the northern hemisphere from 0030 UT to 0106 UT on August 6, 2011, a broad and strong enhancement of Poynting flux in the polar cap latitudes was observed, which is comparable in magnitude to those in the auroral zones. This high-latitude Poynting flux enhancement is associated with the particle precipitation enhancement in the polar cap. Besides the Poynting flux and particle spectra data, the ion convection data were also available for this F16 pass, providing a great opportunity to properly assess the storm event. The particle impact ionization results were put into different atmospheric models (NRLMSISE-00 [Picone et al., 2002], TIE-GCM, and GITM) to examine their geoeffectiveness. The summation of both electron and ion impact ionization rates illustrate the enhanced total ionization in auroral and polar cap regions that is associated with the enhanced Poynting flux during this satellite pass. We further evaluated the importance of particle precipitation in the polar cap, which has been overlooked so far.

3. Methods, Assumptions, and Procedures

3.1 DMSP measurements of particle spectra and Poynting flux

The DMSP F16 satellite has a 101-minute, sun-synchronous, near-polar orbit at 0800-2000 LT at around 830km altitude. In this study, we utilized the measurements from the Precipitating Electron and Ion Spectrometer (SSJ/4), magnetometers (Special Sensor for Magnetic Fields, SSM) and Ion Drift Meter (IDM) on the satellite to obtain particle number fluxes and energy spectra and Poynting fluxes.

The onboard spectrometers measured the precipitating electron and ion fluxes between 30 eV and 30 KeV in 20 channels every second, including10 low-energy channels centered at 34, 49, 71, 101, 150, 218, 320, 460, 670 and 960 eV, and 10 high-energy channels centered at 1.0, 1.4, 2.1, 3.0, 4.4, 6.5, 9.5, 14.0, 20.5 and 29.5 keV. The differential number flux is in unit of (cm2s ster eV)-1, and the differential energy flux is in unit of eV (cm2 s ster eV)-1.

Poynting flux was calculated by combining the velocity and magnetic field measurements as described below: The International Geomagnetic Reference Field (IGRF) magnetic fields and the cross-track velocities in the horizontal and vertical directions, measured by the IDM, were used to calculate the electric fields, with the in-track velocity component ignored. The magnetic field perturbations δB are given by the difference between the vector magnetic field measured by the onboard magnetometer and the IGRF vectors [Huang and Burke, 2004; Knipp et al., 2011; Huang et al., 2013].

3.2 TIE-GCM

The NCAR Thermosphere Ionosphere Electrodynamics Global Circulation Model (TIE-GCM) is a first-principles, three-dimensional, non-linear representation of the coupled thermosphere and ionosphere system. It solves the momentum, energy and continuity equations for neutral and ion species in pressure coordinates [Roble et al., 1988], with a self-consistent calculation of ionospheric wind dynamo effects [Richmond et al., 1992]. The primary external forcings of TIE-GCM are the solar irradiance, magnetospheric energy, and tidal perturbations at the lower boundary of the model. Magnetospheric energy inputs include auroral particle precipitation and high-latitude ion convection.

In this study, the TIE-GCM (version v1.94) was run with a $5° \times 5° \times$half scale height spatial resolution (longitude$\times$latitude$\times$vertical) and 10-minute temporal resolution for the moderate storm on August 5-6, 2011. The solar radiation variability was parameterized by the $F_{10.7}$ index using solar proxy models in different spectral ranges. At the lower boundary, only migrating tidal perturbations were included, which was specified by the Global Scale Wave Model (GSWM) [Hagan and Forbes, 2002; Hagan and Forbes, 2003]. The Weimer [2005] (hereafter Weimer05) potential model was used to specify the high-latitude electric field. The auroral particle precipitation effects were specified using the Roble and Ridley [1987] method for given distributions of precipitating energy fluxes. Note that the parameterization of Roble and Ridley [1987] was designed for a Maxwellian distribution with the energy coverage from approximately a few hundred eVs to about 100 keV. In addition, the precipitation in the cusp

region was specified with a characteristic energy of 100 eV and that of polar rain was specified with a characteristic energy of 500 eV. A uniform energy flux of polar rain was assumed over the polar cap as 0.05 ergs/cm^2/s. The characteristic energy of ion precipitating in the polar cap was assumed to be 10 keV in TIE-GCM. In this study, the ion precipitation was not included for TIE-GCM simulations. As one of the most used GCMs with hydrostatic assumption, the particle impact ionization of TIE-GCM was evaluated through comparisons with the results from the non-hydrostatic GCM, GITM and Fang's parameterization models.

3.3 GITM

The Global Ionosphere-Thermosphere Model (GITM) is a three-dimensional representation of the thermosphere and ionosphere with a spherical grid that can be stretched in latitude and altitude [Ridley et al., 2006]. It uses an altitude-based grid instead of a pressure-based coordinate system like the TIE-GCM. GITM self-consistently solves for the neutral, ion and electron densities, velocities and temperatures, while TIE-GCM solves for mass mixing ratios (mmrs) and assumes the sum of mmrs of N_2, O and O_2 equals 1. GITM solves the vertical momentum equation directly and allows for non-hydrostatic solutions. GITM uses an explicit solver, while other GCMs including TIE-GCM, solve most of the equations implicitly. As a result, GITM runs slowly with a much finer time step of approximately 2 s compared to TIE-GCM, which uses typically a 5-min time step.

GITM is coupled to various models of high-latitude ionospheric electrodynamics. The default electric potential pattern was specified by the Weimer05 model, and the auroral precipitation pattern is described by Fuller-Rowell and Evans [1987]. Fuller-Rowell and Evans [1987] was based on the Television Infrared Observation Satellite Program (TIROS), National Oceanic and Atmospheric Administration (NOAA) measurements and assumes a Maxwellian energy distribution. The ion production rate due to auroral electron precipitation was derived from the formulation described by Frahm et al. [1997]. In this study, GITM was run with a $1^\circ \times 5^\circ$ resolution (longitude $\times$ latitude).

3.4 Fang2010 and Fang2013 Parameterizations for electron and ion impact ionization rates

Fang2010 parameterization was the first parameterization based on first-principle models to provide a fast and accurate method for calculating the altitudinal profiles of ionization rates in the Earth's atmosphere by precipitating monoenergetic electrons in an isotropic angular distribution. It can be applied to any electron precipitation spectra by integrating the contributions of individual monoenergetic components from 100 eV to 1 MeV. In old formulations, incident particles were assumed to have prescribed energy distributions, for example, Maxwellian in Roble and Ridley [1987] and Fuller-Rowell and Evans [1987], which can cause severe errors when the actual spectrum has a significant deviation from the Maxwellian distribution. By decomposing complex energy spectra into contiguous monoenergetic components and applying the parameterization to individual components, Fang2010 enabled ionization calculations for complex particle precipitation in reality. The total ionization is then obtained by summing up the contributions of individual components. To obtain more realistic ionization rate due to electron precipitation in a broad energy range, we applied this Fang2010 parameterization to the complex energy spectra measured by DMSP satellites from 30 eV to 30 keV, instead of applying spectral approximations. Since the lower energy limit of Fang's parameterization is 100 eV, the DMSP measurements with energy lower than 100 eV were not included in the ionization rate calculations.

Although most of the precipitating particle energy into the upper atmosphere is carried by electrons, ion precipitation, specifically, proton precipitation can significantly affect the ionospheric conductance and thermospheric composition. Fang et al. [2013] calculated the primary ionization and secondary electron ionization from precipitating protons through coupling a Monte Carlo proton transport model and a multi-stream electron transport model. And Fang2013 parameterization was derived to provide a fast and accurate method to calculate the total ionization rate from the monoenergetic proton precipitation with energy range from 100 eV to 1 MeV. As Fang2010 parameterization, Fang2013 was applicable to complex incident spectra regardless of the energy distribution. In this study, the parameterization models was applied to the thermosphere simulated by different models: NRLMSISE-00, TIE-GCM and GITM.

4. Results

4.1 DMSP F16 measurements of particle fluxes and Poynting fluxes

In this study, we focused on a DMSP pass over the northern polar region from 0030UT to 0106UT, which is during the main phase of a moderate storm. This storm began on 5 August and continued until August 6, 2011. Figure 1 illustrates the temporal variations of IMF Bz, solar wind dynamic pressure and Dst index during this storm. The storm onset occurred at 1906 UT on 5 August, preceded by a southward IMF of -20 nT. The Dst index reached a minimum of -107 nT around 0300 UT on 6 August. The dashed vertical line indicates the start of DMSP F16 measurements for the northern hemisphere pass from 0030 UT. The horizontal component of ion drift velocity measured by IDM onboard DMSP F16 from 0030 UT to 0106 UT is shown in Figure 2. The magenta vertical lines illustrate the convection reversal boundaries (CRBs), where the ion convection flow changes its direction from sunward (positive in IDM data, typically in the auroral zone) to anti-sunward (negative in IDM data, typically in the polar cap).

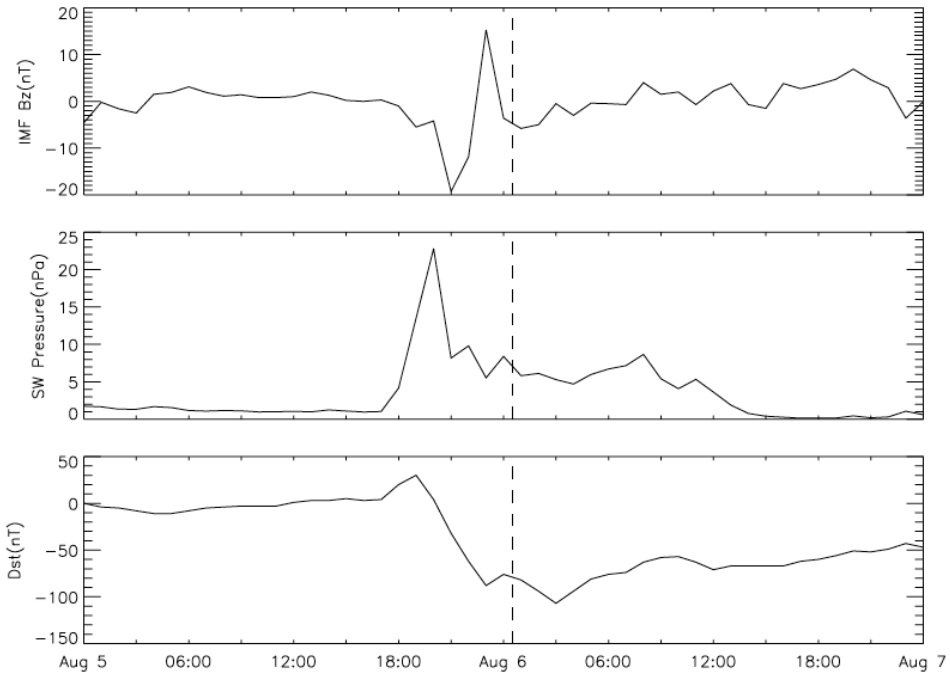

Figure 1. Temporal variations of the IMF Bz, the dynamic pressure of solar wind, and Dst index during a storm occurred on August 6, 2011. *The dashed vertical lines indicate the start of DMSP measurements.*

For this particular F16 pass, the Poynting flux measurement was available as shown in Figure 3. The polar contour depicts the spatial distribution of Poynting flux calculated from Weimer05 model in Altitude Adjustment Corrected Geomagnetic (AACGM) coordinates. The black circle in the upper panel marks the latitude at which the high-latitude electric field is assumed to be zero. The red crosses indicate the projection of the DMSP F16 trajectory. The bottom panel shows the Poynting fluxes along the F16 trajectory measured by the satellite in red and calculated by Weimer05 in black. The two vertical dotted lines indicate magnetic latitude of 45 degrees. The two vertical green lines illustrate the CRBs as the boundary of aurora zones and polar cap region. Although the integration of Poynting flux along the pass gives a close estimate between the model and data, which is around 82 MW/m for F16 and 87 MW/m for Weimer05, the spatial distribution predicted by Weimer05 is quite different from the in-situ F16 measurements in this case. The F16 Poynting flux has three clear peaks at high latitudes, one inside the CRBs and the other two in the auroral zone. Other than these peaks, during this pass of DMSP F16 over the northern hemisphere, a strong and broad Poynting flux enhancement in the polar cap caused by the low-energy electron precipitation was observed but not captured by the model. As an empirical model, Weimer05 is often used to provide the high-latitude forcing to GCMs, and the underestimation of Poynting flux will directly affect the results of GCMs. Therefore, improvements are needed to correctly quantify the Poynting flux distribution particularly when electron precipitation is enhanced.

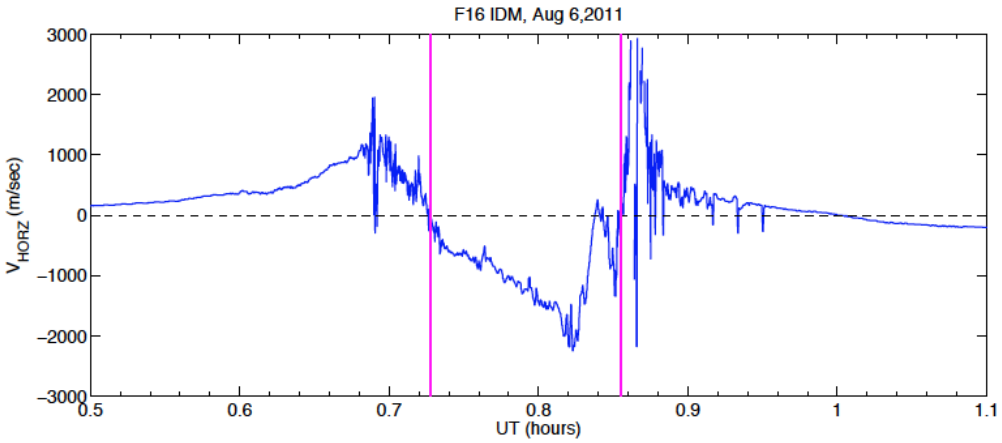

Figure 2. The horizontal component of Ion Drift Meter (IDM) data measured by DMSP F16 from 0030 UT to 0106 UT on August 6, 2011. *The magenta vertical lines illustrate the convection reversal boundaries (CRBs).*

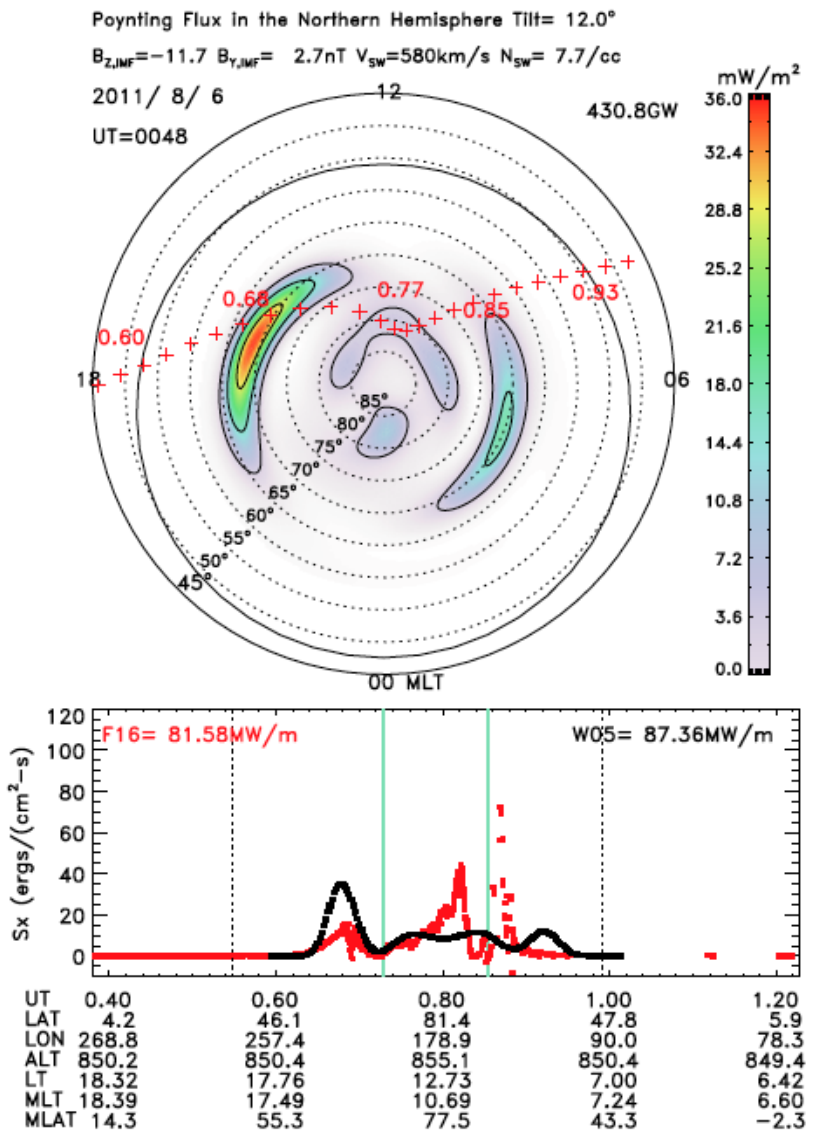

Figure 3. Top: spatial distribution of Poynting flux modeled by Weimer05 around 0050UT on August 6, 2011. *The red crosses indicate the trajectory of F16. Bottom: comparison of Poynting fluxes along trajectory measured by F16 (red) and predicted by Weimer05 (black). The total Poynting fluxes integrated along trajectory are also shown, which is around 82 MW/m for F16, and 87 MW/m for Weimer05. The two vertical green lines indicate the convection reversal boundaries, and the two dotted lines indicate the magnetic latitude of 45 degrees.*

The differential number and energy flux of precipitating electrons measured during this pass are shown in the left column of Figure 4. The two magenta vertical lines indicate the CRBs as in Figure 2. Other than the strong enhancement in the auroral zone, there is also clear enhancement of soft electron fluxes in the polar cap. In particular, the enhancement of electron fluxes with energy below about 300 eV in the polar cap is not negligible compared to the

background intensity. Similarly, the differential number and energy flux of precipitating ions are also shown in the right column of Figure 4. The polar rain region between around 0.73 UT and 0.82 UT can be identified with typically low accompanying ion precipitation. Moreover, left column of Figure 5 shows that the total number flux and the total energy flux of electrons during this F16 pass have significant enhancements in the polar cap region that are sometimes as strong as that in the auroral zone. The mean energies of both electrons and ions are also depicted in the bottom of Figure 5, which was obtained by dividing the total energy flux by the total number flux. The red line indicates the electron energy at 100 eV. The mean electron energy in the polar cap is mostly above 100 eV, while the mean energy of aurora zone is above 1 keV, and those at lower latitudes are mostly below 100 eV. Based on the cusp criteria in Newell and Meng [1988] (Average energy of electrons < 200 eV, average energy of ions < 2700 eV, electron energy flux > eV (cm2 s ster)$^{-1}$, ion energy flux > eV (cm2 s ster)$^{-1}$), we conclude that F16 passed through the cusp region around 0.82 UT, which corresponds to the peak Poynting flux inside CRBs as in Figures 3.

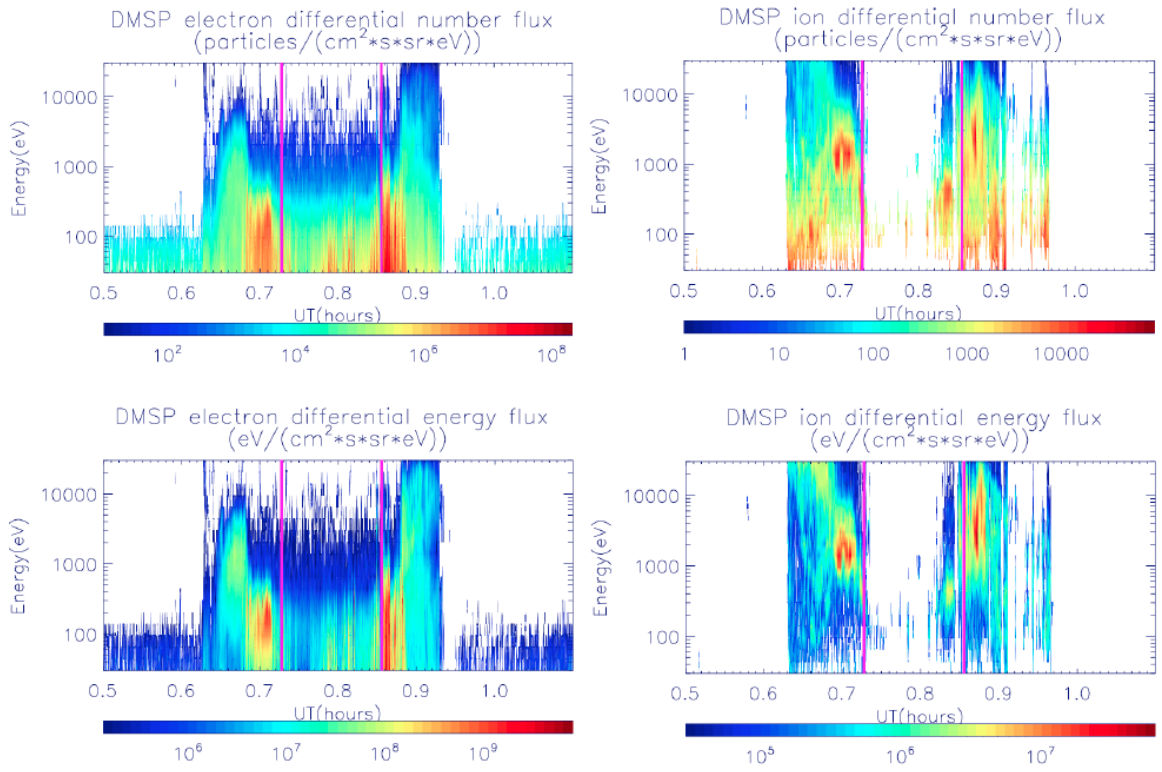

Figure 4. Left column: differential number and energy fluxes of electrons measured by DMSP F16 satellite over the northern hemisphere on August 6, 2011. Right column: differential number and energy fluxes of ions.

The two vertical magenta lines indicate the convection reversal boundaries.

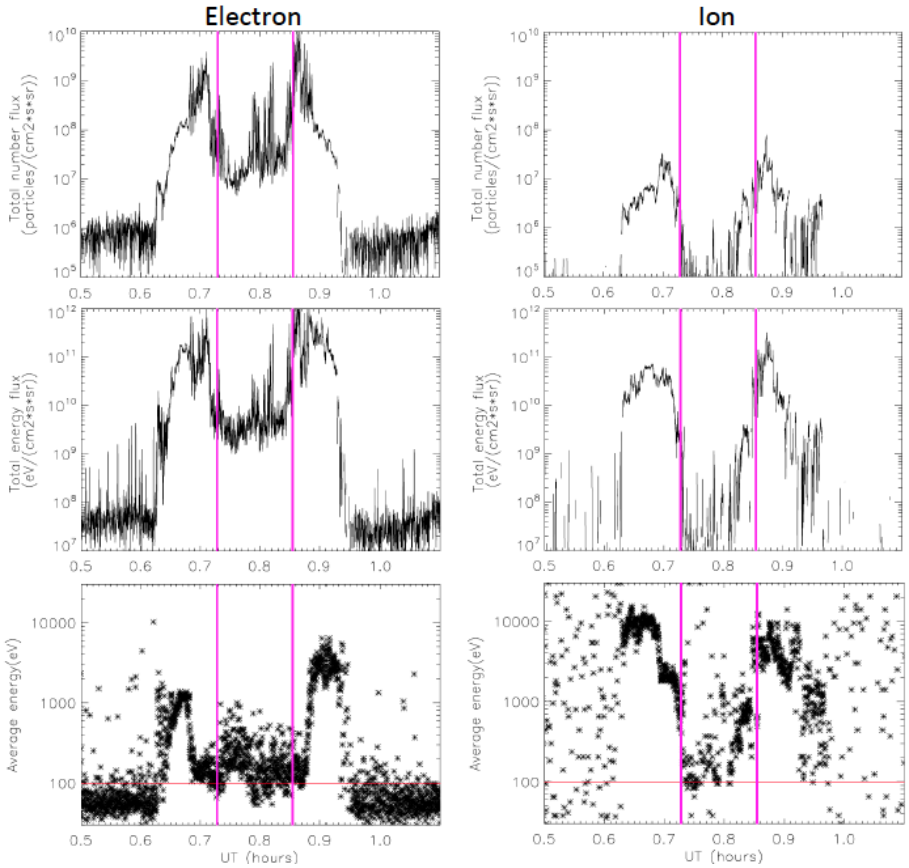

Figure 5. First row: the total number flux of electrons (left) and ions (right) measured by DMSP F16 satellite. The two vertical magenta lines indicate the convection reversal boundaries. Second row: the total energy flux of electrons (left) and ions (right). Third row: the mean energy of electrons (left) and ions (right) obtained through dividing the total energy flux by the total number flux. *The red line illustrates the 100 eV particle energy.*

4.2 Particle impact ionization rates using Fang2010 & Fang2013 parameterizations

Before simulating the ionospheric/thermospheric impact of the observed DMSP electron and ion precipitation, we first examined the neutral density and temperature distributions in the upper atmosphere using three different models: NRLMSISE-00, TIE-GCM, and GITM. NRLMSISE-00 was run with F10.7 of 110 solar flux units (10^{-22}W m^{-2} Hz^{-1}) and Ap index of 100 nT. TIE-GCM and GITM were run with realistic driving conditions and their default electron precipitation models. The left column of Figure 6 depicts altitudinal and temporal variations of the neutral density modeled from NRLMSISE-00, TIE-GCM and GITM, respectively. Due to the high temporal resolution of DMSP measurements (1 second) compared to those of GCMs, the

neutral densities from GCM simulations were sampled at time and location of every DMSP measurement. Similarly, the right column shows the thermospheric temperatures. Figure 6 illustrates that the thermospheric conditions from different models were not quite the same. While the TIE-GCM density is similar to that from NRLMSISE-00, the TIE-GCM temperature is much lower than the other two models. GITM results show a more detailed structure due to its higher temporal and spatial resolution.

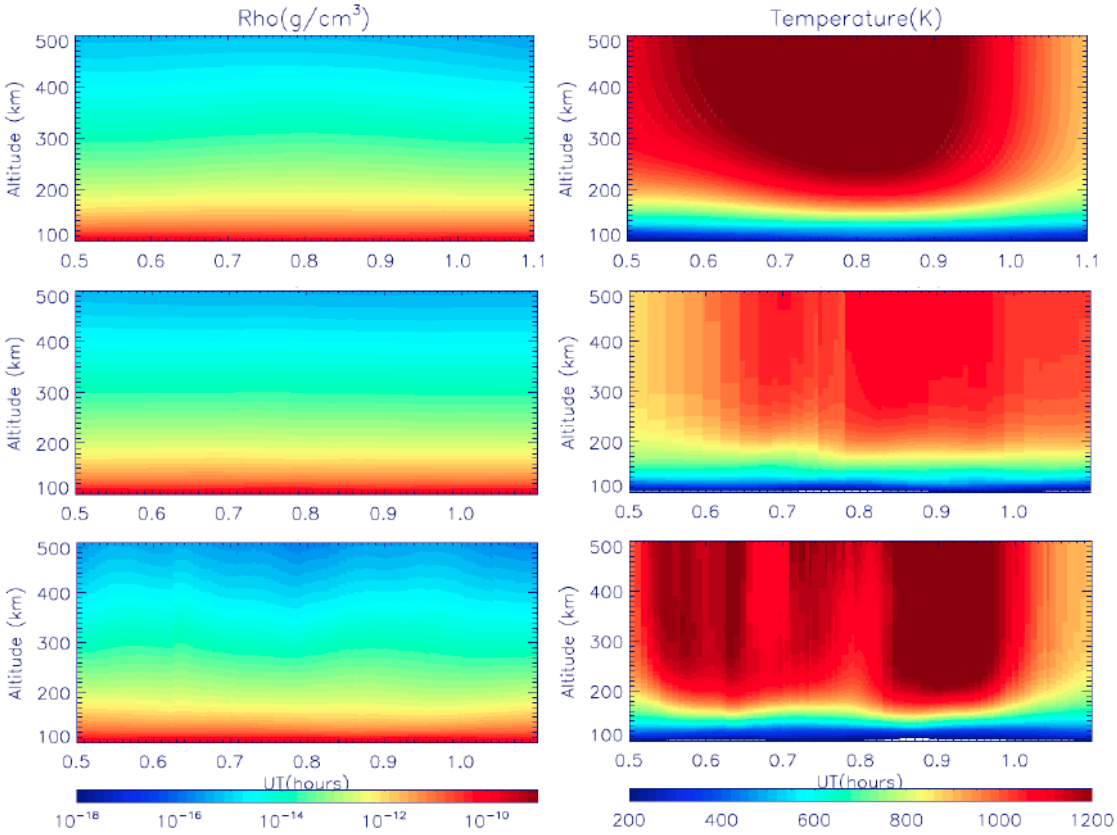

Figure 6. Altitudinal variation of neutral density and temperature along the F16 trajectory from 0030UT to 0106UT simulated by the NRLMSISE-00 model (first row), TIE-GCM (second row) and GITM (third row).

The total particle impact ionization rates obtained from both Fang2010 (for electrons) and Fang2013 (for ions) parameterizations are shown in Figure 7, employing different thermospheric conditions from NRLMSISE-00, TIE-GCM and GITM, respectively. Overall, they have similar configurations and peak magnitudes. All of them show clear enhancement at F-region altitudes in the polar cap region due to the precipitating particles. This localized ionization results in higher electron densities, higher Pedersen conductivities and more Joule heating in the F-region. As

discussed in Huang et al. [2012], the high-altitude F-region Joule heating is more efficient than low-altitude E-region heating in affecting the upper atmosphere. Considering the large area of the polar cap region, the enhanced heating in the F-region polar cap may have a non-negligible influence on the thermosphere at the low-earth-orbit (LEO) around 400 km.

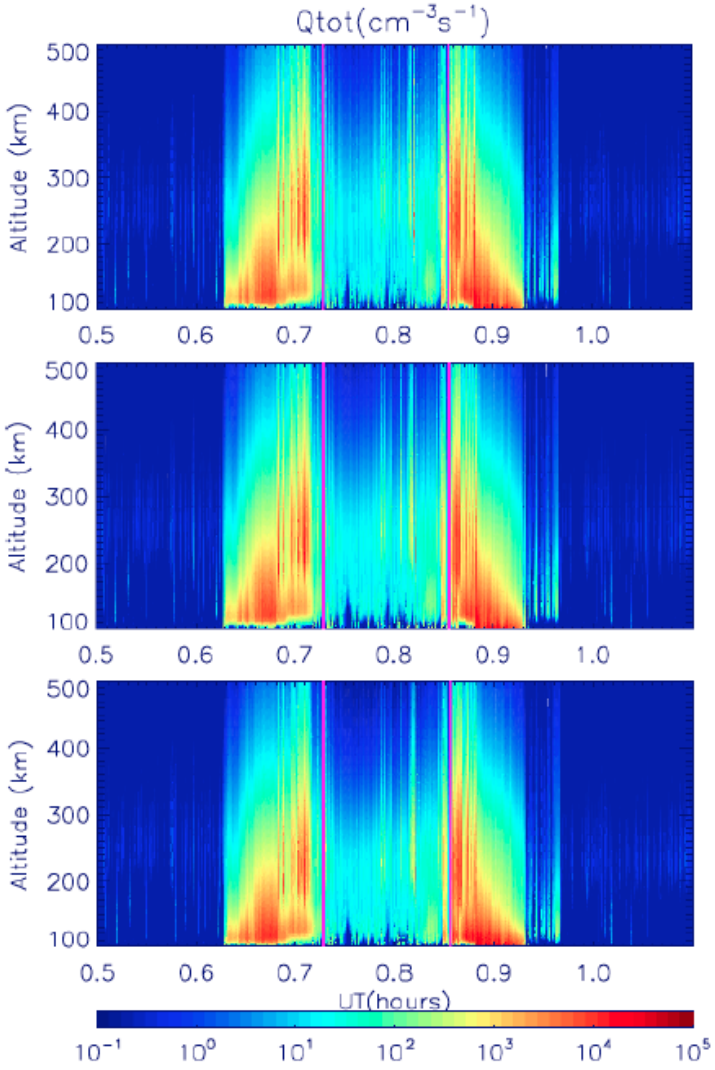

Figure 7. Altitudinal variation of total particle impact ionization rate calculated from Fang2010 (electrons) and Fang2013 (ions) parameterizations along the F16 trajectory using thermosphere simulated by the NRLMSISE-00 model (first row), TIE-GCM (second row) and GITM (third row) in Figure 6. *The two vertical magenta lines indicate the convection reversal boundaries.*

Since there is little effect of model thermosphere to the ionization rate results, we show in Figure 8 the ionization rates due to precipitating electrons (top panel), ions (middle), and their

summation (bottom) using the NRLMSISE-0 thermospheric model. It was noticed that in the polar cap region, majority of ionization at the F-region altitudes is due to electrons, while precipitating ions contribute to significant ionization in the auroral zones with peaks under 200 km. The two peaks above 200 km in the auroral zones are likely associated with the two peaks of Poynting fluxes in the same locations shown in Figure 3. In the polar cap, the broad Poynting flux enhancement corresponds well to the ionization enhancement due to particle precipitations.

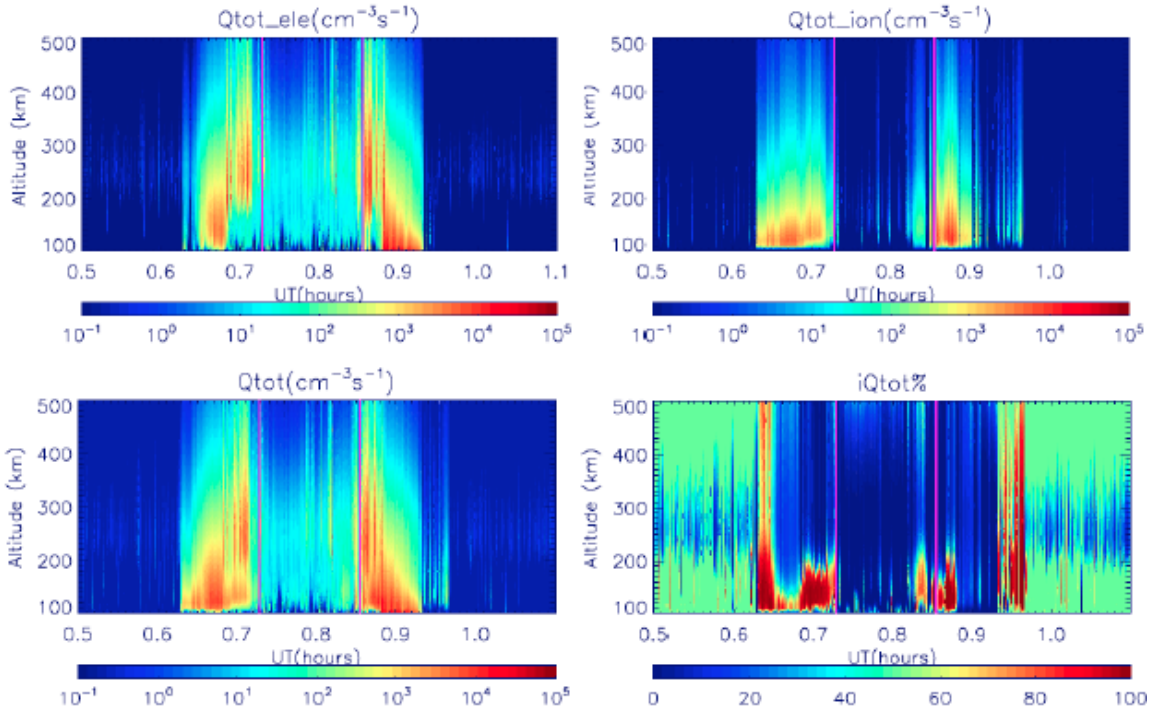

Figure 8. Altitudinal variation of electron impact ionization rate (first row), ion impact ionization rate (second row) and the summation of them (bottom row) along the F16 trajectory using thermosphere simulated by the NRLMSISE-00 model. *The two vertical magenta lines indicate the convection reversal boundaries.*

4.3 Particle impact ionization rates in GCMs

The ionization rate due to precipitating particles is often calculated from empirical models in GCMs as described above. The top panel of Figure 9 depicts the total ionization rate calculated from Fang2010 and Fang2013 parameterizations along with thermosphere simulated by NRLMSISE-00 model and particle spectra measured by DMSP F16 along the satellite tract from 0030 UT to 0106 UT on August 6, 2011. The middle and bottom panels depict the results simulated by TIE-GCM and GITM using their default methods of calculating the particle impact,

which are driven by the geomagnetic indices. Clear ionization enhancements in the auroral zones are illustrated in all panels of Figure 9. However, most of the particle impact ionization is below 200 km in GCMs. In particular, GCMs do not capture the strong ionization enhancements due to low-energy electrons at the F-region altitudes in both auroral zone and polar cap. TIE-GCM result has clear displacements and coarser structures compared to the other two. Whereas GITM shows relatively more detailed structure than TIE-GCM because of its higher resolution, it misses a part of ionization in the polar cap totally. Furthermore, no clear cusp feature is captured by GCMs.

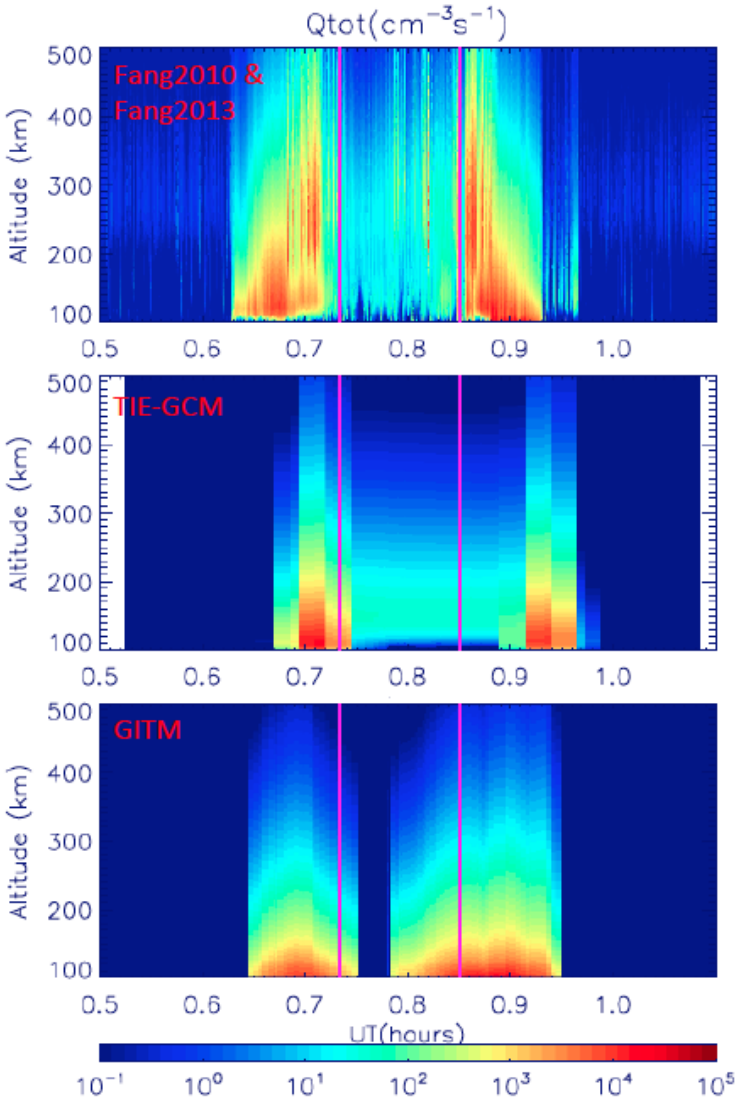

Figure 9. Comparison of total impact ionization rates calculated from (a) Fang2010 and Fang2013 parameterizations, (b) TIE-GCM and (c) GITM along the F16 trajectory for the August 6, 2011 storm.
The two vertical magenta lines indicate the convection reversal boundaries.

The differences between the GCM simulations and Fang2010&Fang2013 can be due to following two factors: **First,** the inputs to the models were different. The inputs to Fang2010&Fang2013 were the particle precipitation from the DMSP observations, whereas the inputs to the GCMs were just empirical formulation driven by the geomagnetic indices. **Second**, the parameterizations for the ionization rates were different. Fang2010&Fang2013 made some improvements, especially for the soft particles, when compared with the empirical models coupled in the GCMs. A significant improvement is needed for accurate parameterization of particle impact ionization in GCMs, such as driving the model with DMSP data or coupling with improved ionization empirical models. The underestimated ionization of GCMs in the polar cap is expected to result in underestimation of electron density, Pedersen conductivity and heating, which are essential to the thermosphere-ionosphere simulation.

5. Conclusion

In this study, we focused on a DMSP pass over the northern polar region, which was during the main phase of the moderate storm occurred on August 6, 2011. The DMSP electron flux measurements show that there is clear enhancement of electron fluxes in the polar cap besides the strong enhancement in the auroral zone. The mean energy in the polar cap is mostly above 100 eV, while the mean energy of aurora zone is above 1 keV, and those in the lower latitudes are mostly below 100 eV. The Poynting flux measured along the DMSP F16 trajectory was quite different compared with the one predicted by Weimer05. Weimer05 gives an incorrect distribution of Poynting flux and F16 captures a strong Poynting flux enhancement in the polar cap caused by the low-energy electron precipitation.

The thermospheric density and temperature have been compared for NRLMSISE-00, TIE-GCM and GITM for this storm. The thermospheric conditions from these models were quite different, however, there was not much difference in particle impact ionization rates calculated using Fang2010 and Fang2013 parameterizations along with these thermospheric conditions. All of them showed a clear enhancement at the F-region altitude in the polar cap region due to the low-energy electrons precipitated, illustrating the importance of widely distributed polar rain and localized cusp soft particle precipitation.

Considering the enhanced ionization and heating in the F-region of large polar cap area the polar rain should have non-negligible influence on the thermosphere during magnetic storms. Using the default empirical formulations of electron impact ionization in GCMs, the result of TIE-GCM does not capture the F-region ionization in the polar cap region shown in Fang2010 results, and GITM misses a part of ionization in the polar cap. The different spatial and temporal distributions of ionization rates from GCMs are due to the difference of both the inputs to the models and the parameterizations of the ionization rates.

REFERENCES

Crowley, G., D. J. Knipp, K. A. Drake, J. Lei, E. Sutton, and H. Lühr, 2010, Thermospheric density enhancements in the dayside cusp region during strong BY conditions, Geophys. Res. Lett., 37, L07110, doi:10.1029/2009GL042143.

Deng, Y., T. J. Fuller-Rowell, A. J. Ridley, D. Knipp, and R. E. Lopez, 2013, Theoretical study: Influence of different energy sources on the cusp neutral density enhancement, J. Geophys. Res. Space Physics, 118, pp. 2340-2349, doi:10.1002/jgra.50197.

Fang, X., C. E. Randall, D. Lummerzheim, S. C. Solomon, M. J. Mills, D. R. Marsh, C. H. Jackman, W. Wang, and G. Lu, 2008, Electron impact ionization: A new parameterization for 100 eV to 1 MeV electrons, J. Geophys. Res., 113, A09311, doi:10.1029/2008JA013384.

Fang, X., C. E. Randall, D. Lummerzheim, W. Wang, G. Lu, S. C. Solomon, and R. A. Frahm, 2010, Parameterization of monoenergetic electron impact ionization, Geophys. Res. Lett., 37, L22106, doi:10.1029/2010GL045406.

Fang, X., D. Lummerzheim, and C. H. Jackman, 2013, Proton impact ionization and a fast calculation method, J. Geophys. Res. Space Physics, 118, pp. 5369-5378, doi:10.1002/jgra.50484.

Frahm, R. A., J. D. Winningham, J. R. Sharber, R. Link, G. Crowley, E. E. Gaines, D. L. Chenette, B. J. Anderson, and T. A. Potemra, 1997, The diffuse aurora: A significant source of ionization in the middle atmosphere, J. Geophys. Res., 102(D23), pp. 28203-28214, doi:10.1029/97JD02430.

Frank, L. A., 1971, Plasma in the Earth's polar magnetosphere, J. Geophys. Res., 76, pp. 5202-5219.

Fuller-Rowell, T. and D. Evans, 1987, Height-integrated Pedersen and Hall conductivity patterns inferred from TIROS–NOAA satellite data, Journal of Geophysical Research 92, p. 7606.

Hagan, M. E. and J. M. Forbes, 2002, Migrating and nonmigrating diurnal tides in the middle and upper atmosphere excited by tropospheric latent heat release, J. Geophys. Res., 107(D24), p. 4754, doi:10.1029/2001JD001236.

Hagan, M. E. and J. M. Forbes, 2003, Migrating and nonmigrating semidiurnal tides in the upper atmosphere excited by tropospheric latent heat release, J. Geophys. Res., 108, p. 1062, doi:10.1029/2002JA009466, A2.

Heikkila, W. J. and J. D. Winningham, 1971, Penetration of magnetosheath plasma to low altitudes through the dayside magnetospheric cusps, J. Geophys. Res., 76, pp. 883-891.

Huang, C. Y. and W. J. Burke, 2004, Transient sheets of field-aligned current observed by DMSP during the main phase of a magnetic superstorm, J. Geophys. Res., 109, A06303, doi:10.1029/2003JA010067.

Huang, C. Y., Y.-J. Su, E. K. Sutton, D. R. Weimer, and R. Davidson, 2013, Energy coupling during the August 2011 magnetic storm, J. Geophys. Res. (submitted).

Huang, Y., A.D. Richmond, Y. Deng, and R. Roble, 2012, Height distribution of Joule heating and its influence on the thermosphere, J. Geophys. Res., 117, A08334, doi:10.1029/2012JA017885.

Knipp, D., S. Eriksson, L. Kilcommons, G. Crowley, J. Lei, M. Hairston, and K. Drake, 2011, Extreme Poynting flux in the dayside thermosphere: Examples and statistics, Geophys. Res. Lett., 38, L16102, doi:10.1029/2011GL048302.

Lazarev, V. I., 1967, Absorption of the energy of an electron beam in the upper atmosphere, Geomagn. Aeron., 7, p. 219.

Luan, X., W. Wang, A. Burns, S. Solomon, Y. Zhang, and L. J. Paxton, 2010, Seasonal and hemispheric variations of the total auroral precipitation energy flux from TIMED/GUVI, J. Geophys. Res., 115, A11304, doi:10.1029/2009JA015063.

Lühr, H., M. Rother, W. Köhler, P. Ritter, and L. Grunwaldt, 2004, Thermospheric up-welling in the cusp region: Evidence from CHAMP observations, Geophys. Res. Lett., 31, L06805, doi:10.1029/2003GL019314.

Newell, P. T. and C.-I. Meng, 1987, Cusp width and Bz : Observations and a conceptual model, J. Geophys. Res., 92(A12), pp. 13673-13678, doi:10.1029/JA092iA12p13673.

Newell, P. T., T. Sotirelis, and S. Wing, 2009, Diffuse, monoenergetic, and broadband aurora: The global precipitation budget, J. Geophys. Res., 114, A09207, doi:10.1029/2009JA014326.

Picone, J.M, A. E. Hedin, D. P. Drob, and A.C. Aiken, 2002, NRLMSISE-00 empirical model of the atmosphere: Statistical comparisons and scientific issues, J. Geophys. Res., 107, A12, p. 1468, doi:10.1029/2002JA009430.

Rees, M. H., B. A. Emery, R. G. Roble, and K. Stamnes, 1983, Neutral and ion gas heating by auroral electron precipitation, J. Geophys. Res., 88(A8), pp. 6289-6300, doi:10.1029/JA088iA08p06289.

Richmond, A. D., E. C. Ridley, and R. G. Roble, 1992, A thermosphere/ ionosphere general circulation model with coupled electrodynamics, Geophys. Res. Lett., 19, 601604.

Ridley, A. J., Y. Deng, and G. Toth, 2006, The Global Ionosphere-Thermosphere Model (GITM). J. Atmos. Solar-Terrestr. Phys., 68, pp. 839-864.

Roble, R. G. and E. C. Ridley, 1987, An auroral model for the NCAR thermospheric general circulation model (TGCM), Ann. Geophys., 5A, p. 369.

Roble, R. G., E. C. Ridley, A. D. Richmond, and R. E. Dickinson, 1988, A coupled thermosphere/ionosphere general circulation model, Geophys. Res. Lett., 15, 13251328.

Weimer, D. R., 2005, Improved ionospheric electrodynamic models and application to calculating Joule heating rates, J. Geophys. Res., 110, A05306, doi:10.1029/2004JA010884.

Winningham, J. D. and W. J. Heikkila, 1974, Polar cap auroral electron fluxes observed with ISIS 1, J. Geophys. Res., 79, pp. 949- 957.

Zhang, Y., L. J. Paxton, and A. T. Y. Lui, 2007, Polar rain aurora, Geophys. Res. Lett., 34, L20114, doi:10.1029/2007GL031602.

LIST OF SYMBOLS, ABBREVIATIONS, AND ACRONYMS

Acronym	Definition
TADs	Traveling Atmospheric Disturbances
GCMs	Global Circulation Models
NCAR	National Center for Atmospheric Research
TIE-GCM	Thermosphere-Ionosphere-Electrodynamics General Circulation Model
GITM	Global Ionosphere Thermosphere Model
DMSP	Defense Meteorological Satellite Program
NRLMSISE-00	Naval Research Laboratory Mass Spectrometer and Incoherent Scatter Radar
SSJ/4	Precipitating Electron and Ion Spectrometer
SSM	Special Sensor for Magnetic Fields
IDM	Ion Drift Meter
IGRF	International Geomagnetic Reference Field
GSWM	Global Scale Wave Model
TIROS	Television Infrared Observation Satellite Program
NOAA	National Oceanic and Atmospheric Administration
CRBs	Convection Reversal Boundaries
AACGM	Altitude Adjustment Corrected Geomagnetic coordinates
LEO	Low-Earth-Orbit

DISTRIBUTION LIST

DTIC/OCP 8725 John J. Kingman Rd, Suite 0944 Ft Belvoir, VA 22060-6218	1 cy
AFRL/RVIL Kirtland AFB, NM 87117-5776	2 cys
Official Record Copy AFRL/RVBXP/Dr. Cheryl Huang	1 cy